Energy Dissipation, Microstructure and Hardening in Cryogenic Machining

C. Saldana
Harold and Inge Marcus Department of Industrial and Manufacturing Engineering
Pennsylvania State University
University Park, PA USA

ABSTRACT
The effects that flood-type cryogenic cooling have on the machining of copper are investigated. Strains of 1-7, strain rates of 1 to 1000 per second and temperatures as low as 77K were used to determine the interactive effects that deformation parameters have on energy dissipation, evolution of microstructure and mechanical properties. It is shown that deformation temperature and strain had the strongest influence on the energy dissipated, while strain rate had a somewhat less significant contribution. Furthermore, a range of severe plastic deformation (SPD) microstructures were developed in the deformed copper depending on the conditions used - these include cellular, elongated, equiaxed and twinned types. These microstructure have direct consequence for understanding the resulting microstructures of the machined surface. These observations offer insights for developing an understanding of the effects that cryogenic cooling have on the energetics of processing, as well on surface integrity.

KEYWORDS
Machining, Cryogenics, Energy, Microstructure

INTRODUCTION

Interest in the use of cryogenic fluids in machining environments has grown significantly. The primary benefit of cryogenic cooling lies in the rapid conduction of heat away from the cutting interface, a primary contributor to conventional tool wear [1-3]. Improved tool wear resistance also is seen due to the relatively higher strength of standard tool materials (e.g., carbide-cobalt alloys and high speed steel) relative to work materials at cryogenic temperatures [1]. In addition to improvements in tool life - this has been shown in Ni- and Ti-alloys, and stainless steels [1, 2] - an added benefit of liquid nitrogen is its tendency to evaporate on contact with the workpiece and tooling. This eliminates the need to manage hazardous waste streams, a common problem for conventional metalworking lubricants [3]. These advantages, extension of tool life and sustainability of processing, are the primary drivers of interest from the machining community in cryogenic cooling technology.

While low cutting zone temperatures are advantageous for the purpose of extending tool life, low temperature can also strongly influence material response during deformation by changing the dominant mechanisms of deformation accommodation at the microscopic level. For example, deformation of low-to-moderate stacking fault energy (SFE) metals typically progresses through the generation and motion of dislocations, their accumulation into cell walls and low angle grain boundaries, followed by grain subdivision and rotation during continuous recrystallization. This process can be expected to occur in a somewhat different manner in the case of low temperature deformation, wherein conventional dislocation cross slip is suppressed and accommodation of plasticity by twinning promoted.

These effects likely modify the specific energy expended during machining and also the mechanical properties and microstructure evolution in the chip material and the machined subsurface. Indeed, the effects of cryogenic cooling on machining performance measures related to surface integrity and forces in select material systems have been explored elsewhere [4-6]. A good example of the effects of cryogenic machining on near-surface microstructures is found in Ref. [4], wherein a region resembling a white layer is observed to form near the machined surface during cryogenic machining of a magnesium alloy.

Our previous work has shown that investigations of the chip microstructure are particularly useful in elucidating the microstructures prevailing on the work subsurface [7], as both share common deformation history in terms of strain, strain rate and temperature. Furthermore, study of the chip materials is also particularly useful for a first-pass understanding of material response during machining, as microstructure studies of the work subsurface generally

require more costly lift-out and removal processes using site specific removal with focused ion beam lithography [8]. In the present study, an understanding of the microstructures evolved during cryogenic machining and their thermo-mechanical properties is developed through analysis of machining chips. This information has importance for understanding the surface layers developed with cryogenic machining.

In the present study, we investigate the influence that cryogenic fluids have on the machining of pure OFHC copper with regard to energy dissipated during processing as well as the integrity of the copper (e.g., microstructure, strength and thermal stability). Copper is a useful model material for face-centered cubic (FCC) metals as its microstructure is highly sensitive to changes in strain, strain rate and temperature.

EXPERIMENTAL PROCEDURE

The work material, OFHC copper (99.99% purity, McMaster-Carr), had an initial grain size of 415 $\pm$ 40 μm and hardness of 72 $\pm$ 5 kg/mm^2. The copper was deformed using a linear machining configuration (Fig. 1), with control of strain possible by adjusting the rake angle of the M2 steel cutting tool between $\alpha = +10°$ and $\alpha = +60°$. The tool was ground sharp (<0.010 mm radius) by grinding the rake and relief faces. The strain rate was, to first order, controlled by varying the deformation rate between V_0 = 0.1 mm/s and V_0 = 200 mm/s. A Kistler dynamometer was used to capture the forces evolved and energy dissipated during cutting. The specific cutting energy was determined by normalizing the energy expended with respect to the sample mass. The width of the workpiece was also made sufficiently large, typically ten times greater than the cutting depth, to reduce the tendency for the deformation to occur out-of-plane (e.g. side-flow) and to thereby ensure a plane-strain condition. The uncut chip thickness (t_0) was approximately 0.2 mm. The side-flow was measured here to be generally less than 2% of the overall cutting width, and the deformed copper samples were typically 0.3 mm × 3 mm × 10 mm in size. To access low deformation zone temperatures, both the work-holding and cutting tool were submerged in a bath of liquid nitrogen (T_0 ~ 77 K).

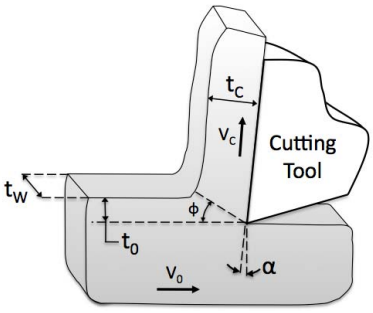

Figure 1. Linear machining configuration used for experiments.

Vickers microhardness measurements were made to characterize the strength of the deformed samples. Thermodynamic behavior was characterized using a Perkin-Elmer Diamond DSC to conduct thermal scans over a range of temperatures (from 323 K to 673 K) at various heating rates (β = 10, 20 and 30 K/min) under an inert atmosphere provided by an N_2 purge gas flowing at 20 mL/min. Stored energy was estimated by integrating the heat flow curve and normalizing this measure with respect to mass. Microstructure was characterized using an FEI Tecnai transmission electron microscope (TEM) at an accelerating voltage of 200 kV. Samples for electron microscopy were mechanically polished to ~ 150 μm thick and thinned in a Struers Tenupol-5 electropolisher using a solution of 33% H_3PO_4 and 67% H_2O at ~ 4.2V and 263 K. Grain size and twin spacing measurements were made following Heyn's line intercept method. A point counting method prescribed by Underwood [9] was used to characterize the twin volume fraction, defined as the fraction of points falling on twinned regions. To reduce the influence of thermal exposure during preparation, hardness measurements and microstructure observations were made within 1 h of deformation and low temperature mounting protocols were used during sample preparation.

RESULTS AND DISCUSSION

Estimation of the deformation parameters (e.g., strain, strain rate and temperature) facilitates generalization of the present results in a framework transferrable to other experimental configurations, including variants of machining (e.g., drilling, turning, grinding) and deformation configurations for cryogenic extrusion, torsion, compression and rolling. Consequently, the mapping of the deformation parameters, e.g., strain, strain rate and temperature, to the controllable input variables, e.g. rake angle and cutting speed, is considered first.

Deformation Parameters

Optical measurement of undeformed and deformed chip thicknesses from 'quickstop' samples enabled rough estimation of the shear strain according to the following Eq. (1), where α is the rake angle and λ is the chip thickness ratio (t_c/t_0) [10].

$$\gamma = \frac{\lambda}{\cos(\alpha)} + \frac{1}{\lambda\cos(\alpha)} - 2\tan(\alpha) \qquad (1)$$

A range of strains can be imposed, with plastic strains of up to 15 being not atypical in the machining of metals such as copper [11, 12]. For the present study, the shear strain at a rake angle of $\alpha = +60°$ was $\gamma \sim 0.8$, this increasing to $\gamma \sim 6.5$ for the most negative rake angle used ($\alpha = +10°$). For the near-cryogenic deformation conditions, only a few samples were created at the lowest shear strain

of $\gamma \sim 0.8$, due to the geometric weakness of the cutting tool at a rake angle of +60° (5° relief). Measurements of the undeformed and deformed chip thicknesses at both cutting speeds (V_0 = 0.1 mm/s and 200 mm/s) and both temperature ranges (T_0 = 77 K and 298 K) confirmed that strain was solely a function of rake angle for the envelope of deformation conditions investigated. The effective strain rate was estimated according to Eq. (2) [10], where Δ is the thickness of the deformation zone,

$$\dot{\varepsilon} = \frac{\gamma V_0}{\sqrt{3}\Delta} \qquad (2)$$

The thickness of the deformation zone was approximated as ~ 100 μm for $V_0 < 100$ mm/s, and ~ 50 μm for $V_0 > 100$ mm/s, in the present deformation of copper. This is following previous characterization of the deformation zone using methods such as PIV, nanoindentation, electron back scatter diffraction (EBSD) and metallography [12-14]. Following Eq. (2), at a deformation rate of 0.1 mm/s, the strain rate ranges between 0.5 to 4 s^{-1} for the strains investigated. At the higher deformation rate of 200 mm/s, the strain rate increases from 2×10^3 to 1.5×10^4 s^{-1}. Hereafter, for convenience, conditions corresponding to V_0 = 0.1 mm/s and 200 mm/s will be referred to as $\dot{\varepsilon} \sim 1$ s^{-1} and $\dot{\varepsilon} \sim 10^3$ s^{-1}, respectively.

The temperature evolved during cutting can be determined by analysis of the force data. Normalizing the dynamometric signal with respect to sample mass facilitated comparison between conditions on the basis of specific cutting energy. Table 1 summarizes the specific cutting energy and its component due to shear for each deformation condition. Under near-ambient/supra-ambient deformation conditions, the cutting energy due to shear increases from approximately 0.274 GPa to 2.450 GPa with increasing strain. This can be compared with deformation at near-cryogenic temperatures, where the shear component increases from 0.455 GPa at the low strain to more than 4.510 GPa at the high strain.

The average temperature rise in the deformation zone ΔT_S can be estimated using thermal analyses that are based on the shear plane model of deformation [10, 15, 16], following Eq. (3),

$$T = \frac{(1-\Gamma)u_s}{\rho c} = \frac{(1-\Gamma)F_s\cos\alpha}{\rho c t_0 t_w \cos(\phi-\alpha)} \qquad (3)$$

$$\Gamma = \frac{1}{4Y}\mathrm{erf}\left(\sqrt{Y}\right) + (1+Y)\mathrm{erfc}\left(\sqrt{Y}\right) - \frac{e^{-Y}}{\sqrt{\pi}}\left(\frac{1}{2\sqrt{Y}} + \sqrt{Y}\right)$$

$$Y = \frac{R\tan(\phi)}{4} \qquad R = \frac{\rho c V_0 t_0}{k}$$

Where u_s is the specific energy due to shear, F_s is the shear force, t_0 is the cutting depth; Γ is the fraction of shear plane heat flowing into the workpiece; c, ρ, and k are the heat capacity, density, and thermal conductivity, respectively, of the workpiece material; F_s is the shear plane component of the resultant force. The specific values of the physical properties for copper are c = 385 J/kg K, ρ = 8900 kg/m^3 and k = 400 W/m K.

The temperature rises in the shear zone, where deformation is accommodated, is provided in Table 1. For deformation at $\dot{\varepsilon} \sim 10^3$ s^{-1} under ambient deformation conditions, the shear plane temperature rise varies from ~ 30 K to 80 K, this consistent with temperature estimates made in the machining of copper at similar strains and strain rates [11]. The time over which the material is exposed to this temperature is on the order of that taken to traverse the deformation zone, approximately 0.1 ms to 10 ms for the deformation conditions used. When deformation occurs at $\dot{\varepsilon} \sim 1$ s^{-1}, the shear plane temperature rise was marginal and the shear zone temperature was near ambient. For the cryogenic conditions, machining was carried out submerged in liquid nitrogen, with the initial temperature of the copper at approximately T_0 = 77 K. The maximum temperature rise for these conditions occurred at the high strain and high strain rate condition, e.g. $\gamma \sim 6.5$ and $\dot{\varepsilon} \sim 10^3$ s^{-1}, this resulting in a maximum shear zone temperature rise of 130 K. At the lower strain, high strain rate conditions, where twinning is indeed more likely to occur in low-to-moderate SFE metals such as copper [17], the shear zone temperature rise is estimated to be between 1 K and 3 K.

Table 1. Specific cutting energy (u_p), specific energy due to shear (u_s) and estimated temperature rise in the shear zone (ΔT_s) as a function of strain, strain rate and initial workpiece temperature.

γ	$\dot{\varepsilon}$ (s^{-1})	T_0 = 298 K			T_0 = 77 K		
		u_p (GPa)	u_s (GPa)	ΔT_s (K)	u_p (GPa)	u_s (GPa)	ΔT_s (K)
1.1	1000	0.475	0.274	29.3	0.860	0.455	48.7
1.6	1000	0.636	0.441	44.1	0.995	0.653	65.4
2.0	1000	0.914	0.693	60.6	1.460	1.031	90.5
3.9	1000	1.890	1.64	74.2	2.241	1.973	89.0
6.5	1000	2.630	2.45	79.7	4.270	3.921	127.7
1.1	1	0.394	0.238	0.7	0.833	0.474	1.4
1.6	1	0.547	0.394	1.1	1.601	0.865	2.3
2.0	1	0.842	0.655	1.5	2.750	1.961	4.5
3.9	1	1.510	1.33	1.4	2.898	2.580	2.8
6.5	1	2.870	2.81	2.2	4.881	4.510	3.5

Thermo-mechanical Measurements

Figure 2 shows the evolution of hardness with increasing strain. For the near-ambient deformation conditions, the hardness increased from ~ 120 kg/mm^2 to ~ 160 kg/mm^2 with increasing strain. The initial steep increase in hardness, which is followed by saturation at higher strains, parallels what has been observed in multi-pass extrusion, multi-pass torsion and single-pass chip formation [11, 12]. Indeed, the saturation of hardness at ~ 160 kg/mm^2 for samples deformed at near-ambient/supra-ambient temperatures is consistent with these earlier works. In contrast, the hardness increased in a similar progression with near-cryogenic temperature deformation, although at a higher level, rising form ~ 145 kg/mm^2 to ~ 190 kg/mm^2 for this range of strains.

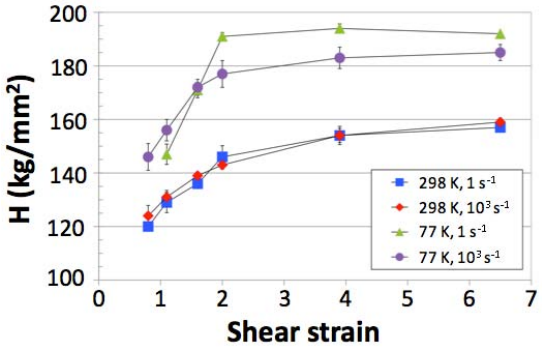

Figure 2. Microhardness of copper deformed at a range of strains, strain rates and temperature conditions.

Cryogenic deformation generally suppresses the mutual annihilation of dislocations by retarding dislocation climb and cross slip, this leading to a higher final defect density and, in the limit, a finer final grain size. This likely contributed to the higher hardness measured at any given strain level when compared with that of ambient deformation. For the entire set of hardness measurements, the variance on the hardness never exceeded 5% of the average hardness value. Non-isothermal calorimetry enables evaluation of transformation characteristics over a wide range of stability and was used here to fingerprint the thermal stability of the deformed copper. Measurements of recrystallization temperature, stored energy, activation energy and reaction kinetics provided a foundation for comparing the deformation conditions on the basis of the relative and absolute thermal stability of the deformed samples, together with the mechanical properties of Fig. 2.

Figure 3 shows representative heat flow curves obtained during non-isothermal annealing of the copper samples at 30 K/min to temperatures exceeding 575 K. At the beginning of each scan, the heat flow is constant, yielding a flat baseline signal. Depending on the amount of prior straining, the heat flow departs from and returns to this constant value after scanning through a range of temperature, yielding a single peak in the thermogram centered on a specific temperature (T_p) and indicative of the occurrence of an exothermic event. Samples annealed a second time through the same temperature range did not again exhibit this peak, suggesting that the transformation was irreversible in nature. An irreversible exothermic transformation for deformed copper in this temperature range (375 K – 550 K) is consistent with recrystallization during non-isothermal annealing of fine-grained copper processed by deformation [18-21]. To confirm that this peak was indeed associated with recrystallization, the hardness of samples annealed to and rapidly quenched from temperatures below and above the peak temperature was measured. From these measurements it is evident that, for the deformation conditions investigated, a dramatic loss in hardness occurs with the evolution of the thermographic peak, this being characteristic of the recrystallization of deformed microstructures.

This single, well-defined exothermic peak is evident for each deformation condition in Fig. 3 and is consistent with the widely-accepted notion that the thermographic peak in the non-isothermal annealing of deformed copper can solely be attributed to recrystallization, with a negligible contribution due to recovery. The recrystallization temperature is usually defined as the temperature where the change in heat flow is zero, e.g. maximum/minimum in heat flow ($d\Phi_m/dt=0$, where Φ_m is the measured heat flow signal), corresponding to the maximal transformation rate. For symmetric thermographic signals, this also corresponds to 50% of the sample volume having been transformed. From the thermograms, this peak recrystallization temperature expectedly shifts to lower temperatures as the strain is increased and the deformation zone temperature is reduced.

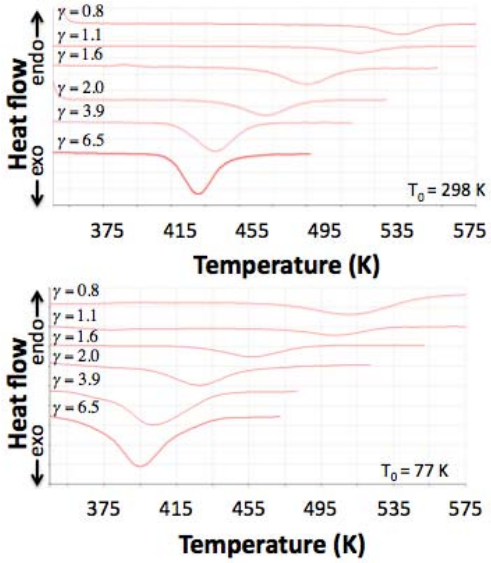

Figure 3. Temperature scans (rate of 30°C/min) of copper deformed at ~ 1 s^{-1} at near-ambient and cryogenic temperatures.

This is more clearly evident in Fig. 4, where the recrystallization temperature measurements for the set of deformation conditions are summarized. For the copper samples deformed in the near-ambient/supra-ambient range of temperatures, the recrystallization temperature decreases with increasing strain from 535 K to 410 K. In contrast, the range of temperature over which the samples deformed at near-cryogenic temperatures recrystallized was approximately 500 K to 350 K. It is also evident that the cryogenically deformed samples have consistently lower recrystallization temperatures than those deformed at similar strains under near-ambient/supra-ambient conditions.

Integration of the peaks in the heat flow curves of Fig. 3, gave a measurement of the stored energy (E), the driving force for recrystallization. The stored energy results are summarized in Fig. 4. For samples deformed under near-ambient/supra-ambient conditions, the stored energy is E ~ 20 J/mol for the low strain conditions, this saturating to E ~ 90 J/mol with increasing strain. This range of stored energy is consistent with other reports that have found a range of 10 – 80 J/mol in copper deformed using other deformation processing routes [18-20]. While this consistency is encouraging for establishing the validity of the present measurements, a unique feature of the current data is the exploration of a higher range of stored energy using the cryogenic deformation protocols. For the cryogenically deformed samples, the stored energy increased from E ~ 50 J/mol to more than E ~ 200 J/mol with increasing strain, the upper portion of this range (> 100 J/mol) having not been previously explored in copper with other deformation routes. Indeed, a higher stored energy for the samples produced by cryogenic deformation is consistent with their higher hardness and lower recrystallization point, presumably due to a greater defect density and smaller grain size that contribute to both strengthening and energy content and generally follow from deformation at low temperatures.

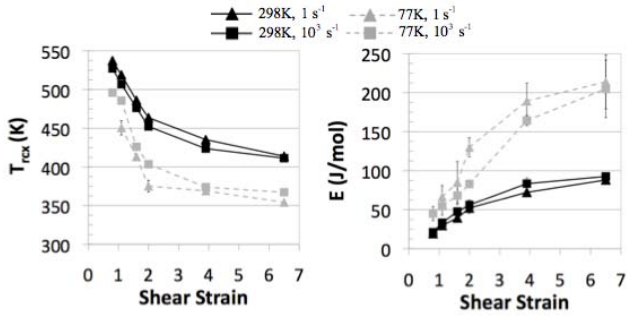

Figure 4. Recrystallization temperature (T_{rcx}) and stored energy (E) of deformed copper as a function of strain, strain rate and temperature.

Deformation Microstructure

Microstructure observation was carried out to elucidate an understanding of the defect structure produced using the various deformation conditions, this having the potential to aid in the screening of possible mechanisms underlying the macro-scale thermo-mechanical response of the deformed copper that was reviewed above. These microstructure observations are provided below and are reviewed separately for each general range of deformation zone temperatures (T_0 = 77 K and 298 K).

Microstructure Evolution with Ambient Deformation

The microstructure development in the copper deformed at near-ambient temperature is shown in Figure 5. Generally, the microstructure evolution between the high and low strain rate samples, points A-D and E-H, respectively, showed little variance between each other; samples produced using either followed the typical development of microstructure with increasing deformation of moderate-to-high SFE FCC metals, as outlined by Hansen [22]. At low strains (γ ~ 0.8 – 1.6, A-B and E-F in the figure), a dense network of dislocations permeated the microstructure. In a few regions, dislocations rearranged to form diffuse cell walls within the pre-existing microcrystalline grain structure; these walls defined cell-type structures, 1 – 2 μm in breadth, with low apparent dislocation contrast in the cell interior. Selected area diffraction (SAD) patterns of large areas (> 4 μm) of these microstructures (see insets) were essentially indistinguishable from that of single-crystal spot patterns, indicative of low misorientation in the microstructure.

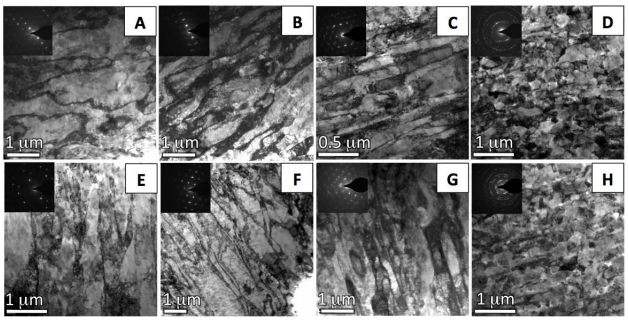

Figure 5. Micrographs showing the evolution of microstructure for copper deformed at near-ambient temperature. Points A through D were deformed at $\dot{\varepsilon}$ ~ 10^3 s^{-1} and at γ ~ 1.1, 1.6, 2 and 3.9, respectively. Points E through H were deformed at $\dot{\varepsilon}$ ~ 1 s^{-1} and at γ ~ 1.1, 1.6, 2 and 3.9, respectively.

At the higher levels of deformation in this range of strains, geometrically necessary boundaries (GNBs), such as dense dislocation walls and microbands, subdivided the cell regions, as is evident for point B. Continued refinement of these GNBs lead to the development of an elongated grain structure characterized by lamellar boundaries, as is evident in the samples deformed to γ ~ 2 (point C). The average distance between these boundaries, as measured perpendicular to the longer boundary dimension, was 207 ±

26 nm for $\dot{\varepsilon} \sim 10^3$ s^{-1} and 347 ± 84 nm for $\dot{\varepsilon} \sim 1$ s^{-1}. The selected area diffraction (SAD) patterns for these samples resembled a smeared single crystal diffraction pattern, indicative of low angle misorientation (< 10°). As with points D and H, increasing strain to $\gamma \sim 3.9$ led to the transformation of this lamellar, elongated microstructure to one characterized by equiaxed grains separated by high angle misorientation. This is evident from the ring-like diffraction that is characteristic of such microstructures in the inset figures. The average grain size for samples deformed at $\gamma \sim 3.9$ with $\dot{\varepsilon} \sim 10^3$ s^{-1} and $\dot{\varepsilon} \sim 1$ s^{-1} was 261 ± 44 nm and 292 ± 73 nm, respectively. The microstructure evolved at higher strains, e.g. $\gamma \sim 6.5$, was not evaluated here. However, other investigations have reported the grain size at $\gamma \sim 7$ to be 261 ± 44 nm at a similar strain rate of $\dot{\varepsilon} \sim 10^3$ s^{-1} [11]. Indeed, this evolution of microstructure, e.g. cells to elongated to equiaxed structures, with saturation of grain size at ~ 250 nm, parallels what has been demonstrated in deformation of copper using extrusion, torsion and machining [11, 12, 18, 23].

Microstructure Evolution with Cryogenic Deformation

The microstructure evolved with cryogenic deformation followed a markedly different progression with strain than that seen above for ambient deformation. Figure 6 shows bright-field and centered dark-field images of the microstructure evolved at $\gamma \sim 0.8$ and $\dot{\varepsilon} \sim 10^3$ s^{-1}. Large areas of the microstructure were seen to consist of long (> 10 μm), straight and finely-spaced boundaries. Furthermore, the SAD patterns inset show evidence of operating reflections in the microstructure. Tilting a specific diffraction condition on to the optic axis and isolating it for imaging with the SAD aperture yielded a centered dark-field image with periodic contrast corresponding to a specific crystal/twin orientation (as in A' and C'). These characteristics give good indication that the adjoining crystals have twinned relationships and the boundaries that separate them are, thus, twin boundaries.

From the micrographs it is also apparent that the microstructure was heterogeneous, with pre-existing grains consisting almost entirely either of deformation twins or the more regular dislocation arrangements (e.g. cells). This is certainly evident in B/B' of Fig. 6, which shows two adjoining grains that have accommodated the deformation in fundamentally different modes. One grain (middle grain of B/B' image pair) is seen to be comprised of a dense network of dislocations arranged in what is likely the start of the formation of a cell wall, this signaling deformation accommodation by conventional slip and glide. The adjoining grain (top-most grain in B/B' micrographs) had a band of twins emanating from the original grain boundary, indicating that mechanical twinning was a more important deformation mode for this particular crystal orientation. Indeed, the nucleation of deformation twins from grain boundaries has been observed elsewhere [24]. The heterogeneity evident in this and, as will be seen below, the other twinned microstructures could be expected due to the strong dependence of twinning probability on the orientation of the loading (shear) direction with respect to the original crystal/grain [25]. For this low strain and high strain rate condition, the twin volume fraction was $V_{twin} \sim 0.62$ and the spacing between twin boundaries was measured to be $d_{twin}(\mu, \sigma) \sim$ (34 nm, 19 nm). This mean spacing is rather characteristic of mechanical (deformation) twinning in copper and is determined primarily due to a material's SFE. As will be seen in the ensuing, the twin boundaries produced by cryogenic deformation at the higher strains ($\gamma \sim 1.1$, 1.6 and 2) and lower strain rates ($\dot{\varepsilon} \sim 1$ s^{-1}) have very similar characteristics to those seen above for $\gamma \sim 0.8$ and $\dot{\varepsilon} \sim 10^3$ s^{-1}.

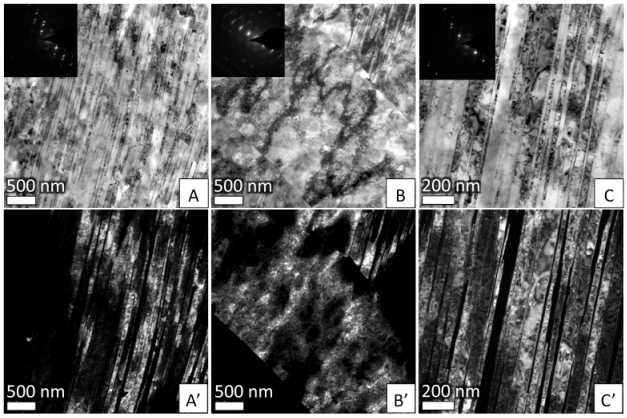

Figure 6. Micrographs showing the evolution of microstructure for copper deformed at cryogenic temperature at $\dot{\varepsilon} \sim 10^3$ s^{-1} and $\gamma \sim 0.8$.

Although the crystallographic and morphological nature of the twins and their formation mechanisms are unlikely fundamentally different at the higher strains and lower strain rates, we detail below observations of the decrease in their relative frequency and, subsequently, increases in their average spacing under such deformation conditions. This is clear in Fig. 7, which shows the continued evolution of the microstructure with strain under cryogenic deformation.

This trend certainly could be expected as continued deformation would promote the creation of defects that, in sufficient quantities, could eventually subsume the pre-existing twin boundaries [20]. In such a situation, the microstructure would ultimately give way to the more prototypical evolution that is characteristic of conventional deformation processing of copper (e.g., cellular to elongated to equiaxed).

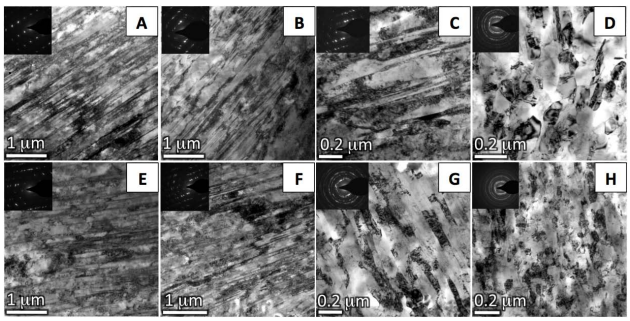

Figure 7. Micrographs showing the evolution of microstructure for copper deformed at cryogenic temperature. Points A through D were deformed at $\dot{\varepsilon} \sim 10^3$ s^{-1} and at $\gamma \sim 1.1$, 1.6, 2 and 3.9, respectively. Points E through H were deformed at $\dot{\varepsilon} \sim 1$ s^{-1} and at $\gamma \sim 1.1$, 1.6, 2 and 3.9, respectively.

As strain is increased to $\gamma \sim 1.1$ at $\dot{\varepsilon} \sim 10^3$ s^{-1} in Fig. 8, the microstructure is quite similar to that seen in Fig. 6 for the lower strain condition. This heterogeneous microstructure is again characterized by a mixture of grains that exhibit either twinning or conventional dislocation slip/glide activity. The A-A' pair of bright-field and centered dark-field images show a microcrystalline grain comprised almost entirely of twin boundaries, while the B-B' pair shows a grain with cellular dislocation structures. The intersection of two such grains is shown in the C-C' pair of images, where across the boundary plane it is evident that deformation is accommodated by fundamentally different modes. For this deformation condition, the twin volume fraction decreased with the increased strain to $V_{twin} \sim 0.4$, with a perceptible increase in the average twin spacing to $d_{twin}(\mu, \sigma) \sim$ (50 nm, 36 nm). A qualitative observation of the grains that did not exhibit twinning is that the dense dislocation walls within the grain interior are beginning to form closed structures, as in B-B' of Fig. 8, evolving from what was mostly open structures in B-B' of Fig. 6. This marks the beginning of the progression of the structure within these particular grains toward the conventional set of deformation microstructures (cellular, equiaxed, elongated).

The microstructure for $\gamma \sim 1.1$ at a lower strain rate ($\dot{\varepsilon} \sim 1$ s^{-1}), as in Fig. 7, is fundamentally similar to that produced at the higher strain rate described above. The twin volume fraction for these conditions, $V_{twin} \sim 0.15$, was substantially lower than that of the microstructure produced at the high strain rate, with the average twin spacing increased further to $d_{twin}(\mu, \sigma) \sim$ (68 nm, 49 nm). As the strain is increased to $\gamma \sim 1.6$ at this same strain rate ($\dot{\varepsilon} \sim 1$ s^{-1}), the volume fraction of twin boundaries falls further to 0.07 and the average twin spacing increases to $d_{twin}(\mu, \sigma) \sim$ (91 nm, 55 nm). Beyond this threshold strain, no further twinning was evident at the low strain rate. In contrast, the microstructure for $\gamma \sim 1.6$ at the higher strain rate ($\dot{\varepsilon} \sim 10^3$ s^{-1}), as in Fig. 7, does retain the heterogeneous mix of twins with cellular structures. This seems to indicate the beginning of cell formation within the twinned areas. Indeed, a gradual transformation of the twinned regions may be expected given the increased numbers of defects created with increasing strain. Accordingly, a decrease in the twin volume fraction to 0.24 is associated with this deformation condition. This is lower than the volume fraction of $V_{twin} \sim 0.4$ at $\gamma \sim 1.1$ and similar strain rate. The average twin spacing remains relatively unaffected at $d_{twin}(\mu, \sigma) \sim$ (45 nm, 22 nm).

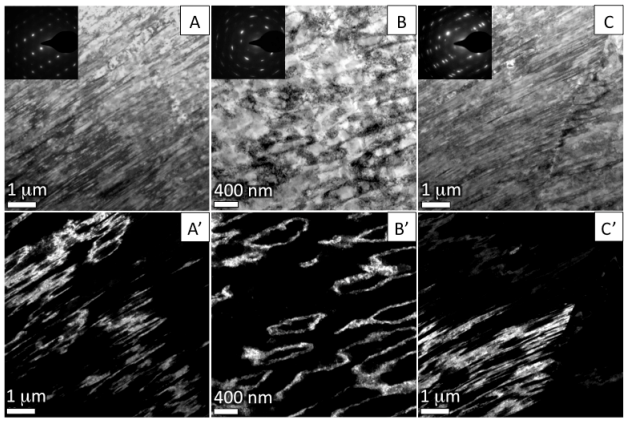

Figure 8. Micrographs showing the evolution of microstructure for copper deformed at cryogenic temperature at $\dot{\varepsilon} \sim 10^3$ s^{-1} and $\gamma \sim 1.1$.

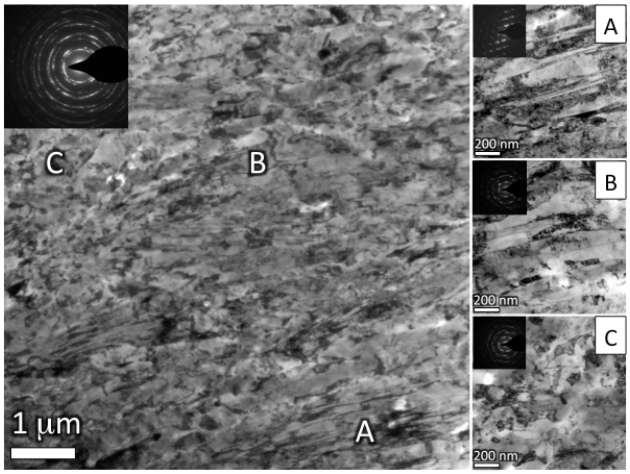

Figure 9. Micrographs showing the evolution of microstructure for copper deformed at cryogenic temperature at $\dot{\varepsilon} \sim 10^3$ s^{-1} and $\gamma \sim 2$.

At higher strains ($\gamma > 2$), the prevalence of twinning in the microstructure is markedly less than for the lower strains, regardless of the strain rate used. The microstructure produced at $\gamma \sim 2$ and $\dot{\varepsilon} \sim 10^3$ s^{-1}, is shown in Fig. 9 and is seen to comprise a heterogeneous mix of twins, elongated boundaries and equiaxed grains. The twin contribution to the overall microstructure is much lower for this condition compared to those described above, as the

twin volume fraction has dropped to $V_{twin} \sim 0.03$ and the twin average spacing risen to $d_{twin}(\mu, \sigma) \sim (73\text{ nm}, 45\text{ nm})$. These twins are seen in inset A and their structure appears quite different than those formed at lower strains, indicating their continued transformation to the other types of defect structures (e.g. cells) with increasing deformation. Indeed, there is an apparent absence of twins at strains in excess of this condition. Other areas of the microstructure are seen to consists of lamellar, elongated boundaries (inset B), similar to the structures seen at an equivalent strain/strain rate combination of parameters at ambient deformation conditions. However, the average width between these structures is smaller at 90 ± 12 nm, as opposed to 207 ± 26 nm for the ambient deformation case. For these regions the SAD pattern appears quite different from that of the twinned areas, with smearing along specific crystal orientations, this indicating low angle misorientation across the boundary plane. Inset C shows the microstructure of select other regions that show even further progression to more equiaxed-type structures. While these are less prominent than the elongated structures at this deformation condition, they too mark the continued evolution of the structure to the equiaxed morphology characteristic of grain structures deformed to high strains, either at ambient or cryogenic. As strain rate is reduced to $\dot{\varepsilon} \sim 1\ s^{-1}$ at a similar strain of $\gamma \sim 2$, the microstructure is relatively homogeneous, almost exclusively comprised of lamellar boundaries as in Fig. 7. These boundaries have an average spacing of 84 ± 17 nm, also much smaller than those created under similar conditions at ambient.

As the strain increases to 3.9, the microstructure evolves qualitatively similar to that of the ambient case, albeit at much smaller length scales, as is evident in Fig. 7. At both strain rates, the elongated, lamellar structure has transformed to an equiaxed morphology with a rather homogeneous microstructure over large areas (> 100 μm^2) visible using the current sample preparation procedure. However, one key difference is that the grain size at $\gamma \sim 3.9$, which was between 250 – 300 nm for the ambient deformation case, was 68 ± 11 nm and 54 ± 11 nm for deformation at $\dot{\varepsilon} \sim 10^3\ s^{-1}$ and $\dot{\varepsilon} \sim 1\ s^{-1}$, respectively.

Table 2. Twin spacing (d_{twin} (μ, σ)) and volume fraction (V_{twin}) measurements of copper deformed at $T_0 = 77$ K.

γ	$\dot{\varepsilon} \sim 1\ s^{-1}$		$\dot{\varepsilon} \sim 10^3\ s^{-1}$	
	V_{twin}	d_{twin} (nm)	V_{twin}	d_{twin} (nm)
0.8			0.62	(34, 19)
1.1	0.15	(68, 49)	0.4	(50, 36)
1.6	0.07	(91, 55)	0.24	(45, 22)
2			0.03	(73, 45)

As was evident from the above discussion, the evolution of microstructure with cryogenic deformation followed a progression quite different, in some respects, to the development seen at near-ambient deformation conditions. Firstly, the presence of dense networks of twin boundaries in the low strain regime (A, B, C, E and F in the figure), and particularly in the low strain, high strain rate regime (A and B), is a unique feature of the cryogenic deformation protocols used herein with machining. The ability to access high strain rates ($\dot{\varepsilon} \sim 10^3\ s^{-1}$) and discretely control strain enabled the creation of samples with high twin volume fractions of $V_{twin} \sim 0.4 – 0.6$. Secondly, a range of microstructure representative of the range accessible by conventional deformation, although at significantly smaller sizes, is seen in D, G and H of Fig. 7. Indeed, the ability to access equiaxed grain diameters of 50 – 70 nm has only been demonstrated with extremely high strains using multi-pass torsion or electrodeposition processes [21, 23].

The twin volume fraction and average twin spacing for the deformation conditions with measurable twin density are summarized in Table 2 for reference. A representative histograms for the twin spacing measurements is provided in Fig. 10. The distribution appears skewed with a log-normal shape, which is also consistent with twin spacing measurements reported elsewhere for mechanical twinning in copper produced by other deformation configurations [26] and those produced under growth processes [27].

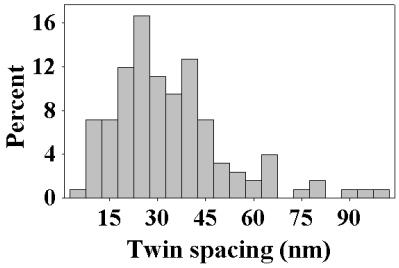

Figure 10. Micrographs showing the evolution of microstructure for copper deformed at cryogenic temperature at $\dot{\varepsilon} \sim 10^3\ s^{-1}$ and $\gamma \sim 0.8$.

CONCLUSIONS

The present study has characterized two important aspects in evaluating the influence of cryogenic fluids on machining applications: the energy dissipated during the process and the integrity of the deformed work material (e.g. strength, stability, microstructure). Appropriate selection of the machining variables (e.g., rake angle, cutting speed, machining temperature) enabled essentially independent selection of deformation parameters to investigate the evolution of these variables. From the present results it is clear that cryogenic cooling can have a marked effect on the machining process and the microstructure of the deformed copper. In terms of energy

dissipated and workpiece integrity (microstructure, strength, stability), it is clear that deformation temperature and strain had the strongest influence, while strain rate had a somewhat less significant contribution.

The range of microstructures observed in the present study includes those considered conventional for deformed copper (e.g., cellular, elongated, equiaxed) as well as the somewhat more unconventional twinned structures. External control of deformation temperature yielded a different size regime for each of the conventional structure types. For example, an equiaxed grain morphology at an ~ 250 nm size scale was accessed during near-ambient deformation while the same structure was created in the 50 – 70 nm range using cryogenic deformation at equivalent strain. A comparison of the micrographs also shows that the same is true for the elongated and cellular microstructure types.

While in the present study, the workpiece was completely immersed in liquid nitrogen, many industrial applications are oriented toward mist-type delivery of liquid nitrogen to the cutting interface. In this regard, the present results describe phenomena that are most likely prevalent for flood-type liquid nitrogen delivery applications. Mist-type applications should result in less severe cooling of the work material, but may exhibit similar effects due to the temperature dependence of material response seen in the present study. Nevertheless, these observations indicate that excessive cooling of the work, which may occur in flood-type delivery of cryogenic fluids, should consider the unintended modifications to material behavior that low-temperature processing engenders.

REFERENCES

[1] Yildiz, Y., Nalbant, M., 2008, A review of cryogenic cooling in machining processes, International Journal of Machine Tools & Manufacture, 48:947–964.

[2] Hong, S. Y., Ding, Y., Jeong, W., 2001, Friction and cutting forces in cryogenic machining of Ti–6Al–4V, International Journal of Machine Tools & Manufacture 41:2271–2285

[3] Pusavec, F., Krajnik, P., Kopac, J., 2010, Transitioning to sustainable production – Part I: application on machining technologies, Journal of Cleaner Production, 18:174–184.

[4] Pu, Z., Outeiro, J. C., Batista, A. C., Dillon, O. W., Puleo, D. A., and Jawahir, I. S., 2012, Enhanced Surface Integrity of AZ31B Mg Alloy by Cryogenic Machining towards Improved Functional Performance of Machined Components, International of Journal Machine Tools and Manufacture, 56:17-27.

[5] Pu, Z., Yang, S., Song, G. L., Outeiro, J. C., Dillon, O. W., Puleo, D.A., and Jawahir, I.S., Ultrafine-grained Surface Layer on Mg–Al–Zn Alloy Produced by Cryogenic Burnishing for Enhanced Corrosion Resistance, Scripta Materiala, 65:520-523.

[6] Pusavec, F., Hamdi, H., Kopac, H. J. and Jawahir, I. S., Surface Integrity in Cryogenic Machining of Nickel-based Alloy – Inconel 718, Journal of Materials Processing Technology, 211:773-783.

[7] Calistes, R., Swaminathan, S., Murthy, T. G., Huang, C., Saldana, C., Shankar, M. R., and Chandrasekar, S., 2009, Controlling gradation of surface strains and nanostructuring by large strain machining, Scripta Materialia, 60:17–20.

[8] Guo, Y., Saldana, C., Compton, W. D., Chandrasekar, S., 2011, Controlling deformation and microstructure on machined surfaces, Acta Materialia, 59:4538.

[9] Underwood, E. E., Coons, W. C., in Reed-Hill R. E., Hirth J. P., Rodgers C., editors. Deformation twinning. New York: Gordon & Breach; 1964.

[10] Shaw, M. C., 1984, Metal Cutting Principles, Oxford University Press, New York.

[11] Brown, T. L., Saldana, C., Murthy, T. G., Mann, J. B., Compton, W. D., Trumble, K. P., King, A. H., and Chandrasekar, S., 2009, A study of the interactive effects of strain, strain rate, and temperature in severe plastic deformation of copper, Acta Materialia, 57:5491-5500.

[12] Swaminathan, S., Shankar, M. R., Lee, S., Hwang, J., King, A. H., Kezar, R., Rao, B. C., Brown, T. L., Chandrasekar, S., Compton, W. D., and Trumble, K. P., 2005, Large strain deformation and ultra-fine grained materials by machining, Materials Science and Engineering A, 410:358–363.

[13] Keciouglu, D., 1958, Shear-strain rate in metal cutting and its effects on shear-flow stress, Transactions of the ASME, 80:158–168.

[14] Oxley, P. L. B., 1989, Mechanics of Machining, Ellis Horwood, New York.

[15] Boothroyd, G., 1963, Temperatures in orthogonal metal cutting, Proceedings of the Institution of Mechanical Engineers, 177, pp. 789–810.

[16] Weiner, J. H., 1955, Shear-plane temperature distribution in orthogonal cutting, Transactions of the ASME, 77:1331–1341.

[17] Saldana, C., Murthy, T. G., Shankar, M. R., Stach, E. A. and Chandrasekar, S., 2009, Stabilizing nanostructured materials by coherent nano-twins and their grain-boundary triple junction drag, Applied Physics Letters, 94:021910.

[18] Jiang, H., Zhu, Y. T., Butt, D. P., Alexandrov, I. V., and Lowe, T. C., 2000, Microstructural evolution, microhardness and thermal stability of HPT-processed Cu, Materials Science and Engineering A, 290:128.

[19] Li, Y. S., Zhang, Y., Tao, N. R. and Lu, K., 2009, Effect of the Zener–Hollomon parameter on the microstructures and mechanical properties of Cu subjected to plastic deformation, Acta Materialia, 57:761.

[20] Lu, L., Dao, M., Zhu, T. and Li, J., 2009, Size dependence of rate-controlling deformation

mechanisms in nanotwinned copper, Scripta Materialia, 60:1062.

[21] Gunther, B., Kumpmann A. and Kunze, H. D., 1992, Secondary recrystallization effects in nanostructured elemental metals, Scripta Metallurgica et Materialia, 27:833.

[22] Hughes, D. A. and Hansen, N., 1997, High angle boundaries formed by grain subdivision mechanisms, Acta Materialia, 45:3871.

[23] Liao, X. Z., Zhao, Y. H., Zhu, Y. T., Valiev, R. Z. and Gunderovm, D. V., 2004, Grain-size effect on the deformation mechanisms of nanostructured copper processed by high-pressure torsion, Journal of Applied Physics, 96:636.

[24] Han, W. Z., Wu, S. D., Li, S. X. and Zhang, Z. F., 2008, Origin of deformation twinning from grain boundary in copper, Applied Physics Letters, 92:221909.

[25] Christian, J. W. and Mahajan, S., 1995, Deformation twinning, Progress in Materials Science, 39:1.

[26] Tao, N. R. and Lu, K., 2009, Nanoscale structural refinement via deformation twinning in face-centered cubic metals, Scripta Materialia, 60:1039.

[27] Shen, Y. F., Lu, L., Lu, Q. H., Jin Z. H., and K. Lu, 2005, Tensile properties of copper with nano-scale twins, Scripta Materialia, 52:989.